Experimental Mechanics
https://doi.org/10.1007/s11340-018-00457-0

Augmented Lagrangian Digital Image Correlation

J. Yang[1] · **K. Bhattacharya**[2]

Received: 19 February 2018 / Accepted: 9 November 2018

Abstract
Digital image correlation (DIC) is a powerful experimental technique for measuring full-field displacement and strain. The basic idea of the method is to compare images of an object decorated with a speckle pattern before and after deformation, and thereby to compute the displacement and strain fields. Local subset DIC and finite element-based global DIC are two widely used image matching methods. However there are some drawbacks to these methods. In local subset DIC, the computed displacement field may not be compatible, and the deformation gradient may be noisy, especially when the subset size is small. Global DIC incorporates displacement compatibility, but can be computationally expensive. In this paper, we propose a new method, the augmented-Lagrangian digital image correlation (ALDIC), that combines the advantages of both the local (fast) and global (compatible) methods. We demonstrate that ALDIC has higher accuracy and behaves more robustly compared to both local subset DIC and global DIC.

Keywords Digital image correlation (DIC) · Augmented Lagrangian

Introduction

Digital image correlation (DIC) is a popular optical experimental technique for measuring deformation and strain in solids. In this method, we take a sequence of grayscale digital images of a test specimen decorated with a speckle pattern during deformation. Then, by comparing images in the sequence, we determine the displacement and strain fields of the specimen using image tracking algorithms [1–4]. It has several advantages compared with other strain measurement methods. It does not require contact with the specimen (especially advantageous for soft materials where contact may affect strain fields) and provides full field displacement and strain values unlike electrical resistance strain gauges and extensometers. Further, compared with other non-contact and full field optical strain measurement methods such as holographic methods and interferometric methods [5–8], DIC does not require a very sophisticated experimental environment.

✉ K. Bhattacharya
bhatta@caltech.edu

[1] Department of Mechanical Engineering, University of Wisconsin, Madison WI 53706, USA

[2] Division of Engineering and Applied Science, California Institute of Technology, Pasadena, CA 91125, USA

This has led to the wide use of DIC as illustrated by the following examples. DIC has been applied to study the behavior of diverse solids systems such as biological material [9–11], metal alloys [12], shape memory alloys [13], porous metals [14], polymers [15], and polymer foams [16]. It has provided insights into very nonlinear behavior of solids like slip bands [13, 17] and crack tips [18]. This method can also be combined with other diagnostic tools to enable investigation of complex phenomena with very heterogenous and complex strain fields at various length scales from kilometers to nanometers. DIC has been used to measure nonuniform phase transformation by combining scanning electron microscopy (SEM) and electron backscatter diffraction (EBSD) [19]. It has also been used with atomic force microscopy (AFM) to measure in-plane displacement at the nanometer scale [20]. At the other extreme, DIC has been used in earthquake and glacier monitoring [21–23] at the scale of tens of kilometers.

Over the last thirty years, various DIC algorithms to compare images and to obtain displacement and strain have been proposed and implemented. Most algorithms can be cast into two categories: local subset DIC method and global DIC method [24–28]. In local subset DIC, as its name implies, we first break up both reference image and deformed image into many subsets and then find the deformation of each subset independently. Since the subsets are limited in size, the deformation of each subset can be solved very fast; moreover, the subsets can be

Published online: 06 December 2018

analyzed in parallel. Therefore, local subset DIC can be very fast. However, since the deformation of each subset is obtained independently, the overall deformation may not be compatible and the strain field can be extremely noisy. In global DIC, we represent the global deformation using a basis set (often based on a finite element discretization), and then analyze the global image to obtain the coefficients relative to this basis set. However, this is expensive.

These considerations have led to a number of attempts to improve these methods. A number of filtering and smoothing schemes have been proposed to address the noisiness of the local subset DIC methods [29–31]. Broadly, filtering of both the images and the displacements not only reduces the noise but also can improve the accuracy because it incorporates information from surrounding regions. While this can be effective, the critical choice of filter is unrelated to the underlying mathematical structure and may be experiment dependent. Similarly, a number of sophisticated numerical methods have been introduced to address the computational cost of global methods. These have followed two key ideas, or a combination of the two. The first is to use either gradient [32] or elastic [33–35] regularization. The second is to use domain decomposition where the domain is broken up into a number of sub-domains, the correlation is performed compatibly in each sub-domain and the compatibility between the sub-domains is enforced using either Lagrange multipliers [34, 36] or the finite element tearing and interconnecting (FETI) procedure [33, 35]. These can then be used in parallel implementation (see [37] for a review). These significantly speed up the convergence and reduce computational time. However, these require sophistication in their implementation and must be adopted to the problem at hand.

In this paper, we propose and demonstrate a new image comparison algorithm: augmented Lagrangian DIC or ALDIC. This method seeks to combine the advantages of both the local subset DIC (speed and parallel implementation) and the global DIC (displacement compatibility and strain smoothness). The basic idea is to match subsets locally as in the local subset DIC, but use compatibility as a constraint. Specifically, we introduce an auxiliary globally compatible displacement field and introduce the constraint that this auxiliary globally compatible displacement field and its gradient equal the locally correlated values. We implement the constraint using the augmented Lagrangian method.

The augmented Lagrangian method, also known as the method of multipliers, has been used to solve constrained minimization problems in diverse fields [38, 39]. It adds to the objective functional a term that is linear in the constraint as in the method of Lagrange multipliers and a term that is quadratic in the constraint as in the penalty method. The addition of the quadratic term makes the numerical implementation easier than the method of Lagrange multipliers. However, unlike the penalty method, one does not need to take the limit of infinitely large penalty coefficients. For this reason, the augmented Lagrangian method has found widespread acceptance in both image precessing [40] and in mechanics [41, 42].

We implement the augmented Lagrangian using the alternating direction method of multipliers (ADMM) that is a form of operator splitting [43]. In this method, we successively perform the local correlation, optimize the auxiliary displacement, update the multiplier and iterate. The convergence and other numerical issues of ADMM have been carefully studied [44], and this method is widely used in image processing [43, 45, 46] and in mechanics [47]. The second problem, the optimization over the auxiliary displacement, is global. However, it leads to a universal, sparse, well-conditioned operator (sum of the Laplacian and identity). This can be treated very efficiently using established methods.

We begin by providing some background into DIC in "Background" and reviewing local and global DIC methods in "Local Subset DIC Method" and "Global DIC Method" respectively. We formulate augmented Lagrangian DIC or ALDIC and describe its implementation in "Augmented Lagrangian DIC (ALDIC) Method". We verify and evaluate the accuracy of the proposed method using a series of case studies using synthetic data from the Society of Experimental Mechanics DIC challenge "Case Study I: Synthetic Images from the SEM 2D-DIC Challenge" and from a current experiment "Case Study II: Experimental Heterogeneous Fracture Deformation". These examples demonstrate the superior accuracy of the proposed algorithm. We analyze the efficiency of the proposed method in "Computational Cost". We show that the computational effort of the ALDIC is at worst a factor of two to four more expensive compared to local subset DIC, and less expensive than global DIC.

Background

Digital Image Correlation as an Optimization Problem

Consider a domain $\Omega \subset \mathbb{R}^n$ undergoing a deformation $\mathbf{y} : \Omega \to \mathbb{R}^n, (n = 2, 3)$. As seen in Fig. 1, let $\mathbf{X}$ denote

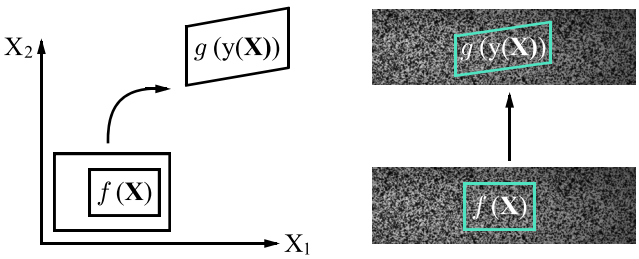

Fig. 1 DIC reference image $f(\mathbf{X})$ deforms into deformed image $g(\mathbf{y}(\mathbf{X}))$

the reference or undeformed position of a particle in Ω and $\mathbf{y}(\mathbf{X})$ denote the deformed or current position of the particle. Suppose we have a speckle pattern with grayscale value $f(\mathbf{X})$ in the reference domain, and the corresponding grayscale value $g(\mathbf{y})$ in the current configuration. If the deformation convects the grayscale, then we have

$$f(\mathbf{X}) = g(\mathbf{y}(\mathbf{X})). \tag{1}$$

The problem of digital image correlation is the *inverse problem* of finding the deformation $\mathbf{y}(\mathbf{X})$ that satisfies (1) given grayscale images $f(\mathbf{X})$ and $g(\mathbf{y})$. We pose it as one of optimization, or one of finding the deformation map that minimizes the squared difference:

$$C = \int_{\Omega} |f(\mathbf{X}) - g(\mathbf{y}(\mathbf{X}))|^2 \, d\mathbf{X} \rightarrow \text{minimize over } \mathbf{y} : \Omega \rightarrow \mathbb{R}^n. \tag{2}$$

A few comments are in order. First, the images are pixelated with f, g taking discrete values. So we can either replace the integrals above with a sum, or interpolate the images (we use bi-cubic interpolation whenever we need sub-pixel values). Second, due to illumination artifacts and gain errors in real experiments, it is useful to normalize the images. This normalization depends on the knowledge of illumination and other experimental details. A simple example is to normalize both images to have the same mean and standard deviation:

$$f(\mathbf{X}) \mapsto \frac{f(\mathbf{X}) - \bar{f}}{\sigma_f}, \quad g(\mathbf{y}) \mapsto \frac{g(\mathbf{y}) - \bar{g}}{\sigma_g} \tag{3}$$

where $\bar{f}, \bar{g}$ are the mean values of f, g, and σ_f, σ_g are their standard deviations [48]. Henceforth, we assume that we are always working with normalized images. Third, in light of the normalization, note that minimizing C is equivalent to maximizing the cross correlation

$$\int_{\Omega} f(\mathbf{X}) g(\mathbf{y}(\mathbf{X})) d\mathbf{X}. \tag{4}$$

Finally, in practice, there are different ways in which the correlation can be performed. One can take a series of images as the deformation proceeds and do the correlation between consecutive images, or one correlate the first and final image, or one can do something intermediate. The incremental correlation between successive image can lead to easier convergence and smaller individual errors due to small displacement, but can lead to the accumulation of systemic errors and can add to the cost. These issues are common to all three algorithms that we discuss presently.

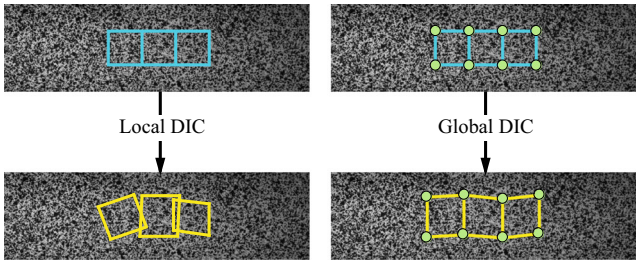

Fig. 2 Comparision between Local and global DIC

Local Subset DIC Method

The local subset DIC method is the most widely used algorithm in DIC software packages [25, 26, 28]. As the name indicates, the idea is to break up the domain into local subsets and perform the correlation or optimization independently in each subset (see Fig. 2, left). Mathematically, we break up our domain into a finite number of subsets $\Omega = \bigcup_i \Omega_i$, and make the ansatz that the deformation is piecewise affine

$$\begin{aligned} \mathbf{y}(\mathbf{X}) &= \mathbf{X} + \mathbf{u}(\mathbf{X}) \\ &= \mathbf{X} + \sum_i (\mathbf{u}_i + \mathbf{F}_i(\mathbf{X} - \mathbf{X}_{i0}))\, \chi_i(\mathbf{X}) \end{aligned} \tag{5}$$

where $\mathbf{X}_{i0}$ is the center of local subset Ω_i, $\mathbf{u}_i$ is the displacement of $\mathbf{X}_{i0}$ and $\mathbf{F}_i$ is the uniform displacement gradient of Ω_i and χ_i is the characteristic or index function

$$\chi_i = \begin{cases} 1 & \mathbf{X} \in \Omega_i, \\ 0 & \mathbf{X} \notin \Omega_i. \end{cases} \tag{6}$$

The optimization problem (2) decomposes into a number of decoupled problems of optimizing over six ($n = 2$) or twelve ($n = 3$) scalar variables:

$$C_i = \int_{\Omega_i} |f(\mathbf{X}) - g\,(\mathbf{X} + \mathbf{u}_i + (\mathbf{F}_i(\mathbf{X} - \mathbf{X}_{i0})))|^2 \, d\mathbf{X} \rightarrow \text{minimize over } \mathbf{F}_i, \mathbf{u}_i. \tag{7}$$

There are a number of methods that have been used to solve this problem including the Inverse Compositional Gauss-Newton(IC-GN) scheme [24, 25, 49] and Inverse Compositional Levenberg-Marquardt(IC-LM) scheme [49]. In this paper, we use IC-GN and this is described in detail in Appendix A and summarized in Algorithm 1. Additionally, there are methods based on the fast Fourier transform.

Since the problems are decoupled, i.e., can be solved independently for each i, local subset DIC is extremely fast and easily paralellized. Further, in practice, the subsets can overlap. However, since each problem is solved

independently, the results can be noisy, susceptible to local imaging problems and lead to discontinuous strain fields.

Algorithm 1 Local subset DIC

Input: Reference image f, deformed image g
Output: Displacement $\mathbf{u}_i$, affine deformation gradient tensor $\mathbf{F}_i$ of each local subset
Step 1: Initialization using FFT integer pixel search method;
Step 2: Precompute image gradients ∇g;
Step 3: For each local subset, compute a_{ip}, b_{iqr}, c_{jkqr} using (31), (32), (33);
while $\|d_i\|, \|e_{jk}\| > \varepsilon$ **do**
  Step 4: Warp deformed image g with current deformation $\mathbf{F}_i, \mathbf{u}_i$;
  Step 5: Compute d_i, e_{jk} using (34), (35);
  Step 6: Compute $\mathbf{v}$, $\mathbf{H}$ using (30) ;
  Step 7: Update ϕ using (28)
end

Global DIC Method

In the global DIC method, we represent the global deformation using a global basis set, often based on a finite element discretization, such that the compatibility or continuity of displacement is guaranteed automatically (see Fig. 2, right):

$$\mathbf{y}(\mathbf{X}) = \mathbf{X} + \mathbf{u}(\mathbf{X}) = \mathbf{X} + \sum_p u_p \boldsymbol{\psi}_p(\mathbf{X}) \tag{8}$$

where $\boldsymbol{\psi}_p(\mathbf{X})$ are the chosen global basis functions and u_p are the unknown degrees of freedom. Thus, the problem (2) becomes

$$C_g = \int_\Omega \left| f(\mathbf{X}) - g(\mathbf{X} + \sum_p u_p \boldsymbol{\psi}_p(\mathbf{X})) \right|^2 d\mathbf{X} \rightarrow \text{minimize over } \{u_p\}. \tag{9}$$

We can solve this problem iteratively by setting $\mathbf{u}_{k+1} = \mathbf{u}_k + \delta\mathbf{u}$ and using the first order approximation

$$g(\mathbf{y}(\mathbf{X})) = g(\mathbf{X} + \mathbf{u}_k(\mathbf{X}) + \delta\mathbf{u}) \approx g(\mathbf{X} + \mathbf{u}_k(\mathbf{X})) + \nabla g \cdot \delta\mathbf{u}(\mathbf{X}) \tag{10}$$

so that

$$C_g \approx \int_\Omega \left| f(\mathbf{X}) - g(\mathbf{X} + \mathbf{u}_k(\mathbf{X})) - \left(\sum_p \delta u_p \boldsymbol{\psi}_p(\mathbf{X}) \right) \cdot \nabla g(\mathbf{X}) \right|^2 d\mathbf{X}. \tag{11}$$

This leads to the linear equation in $\delta\mathbf{u}$

$$M_{pq} \delta u_q = b_p, \tag{12}$$

where

$$M_{pq} = \int_\Omega \boldsymbol{\psi}_p^T(\mathbf{X}) \, (\nabla g) \, (\nabla g)^T \, \boldsymbol{\psi}_q(\mathbf{X}) d\mathbf{X}, \tag{13}$$

$$b_p = \int_\Omega \left(f(\mathbf{X}) - g(\mathbf{X} + \mathbf{u}_k(\mathbf{X})) \right) \boldsymbol{\psi}_p^T(\mathbf{X}) \nabla g(\mathbf{X}) d\mathbf{X}. \tag{14}$$

In this paper, we use a Q4 finite element mesh in global DIC, and the algorithm is summarized in Algorithm 2. Alternately, if the displacements are small, we can treat (12) as a linear problem with $\delta\mathbf{u}$ as the incremental displacement.

Note that the size of the linear problem (12) is equal to the number of basis functions or the size of the finite element discretization. This can be large if we seek fine resolution. Thus, global DIC is expensive and difficult solve in parallel. However, it leads to compatible solutions. And there are methods to reduce the computational expense as discussed in the introduction. In practice, it is common to replace ∇g with ∇f or to use IC-GN which deals with the inverse map. This has the advantage that the matrix M_{pq} is independent of iteration thereby reducing the effort.

We remark that the procedure described in Eqs. 12–14 may result in noisy displacement fields because of the conditioning of the matrix M. So it is common practice to add a weighted higher order penalty (regularizer) to the objective function. This needs experience and expertise. Further, this requires boundary conditions whose choice can lead to errors. Finally, note that the global DIC is not limited to smooth fields. It can be used to study discontinuous fields like cracks and shear bands by using enriched basis [50, 51].

Algorithm 2 Q4 global DIC

Input: Reference image f, deformed image g
Output: Displacement $\mathbf{u}$
Step 1: Initialization using FFT integer pixel search method;
Step 2: Precompute image gradients ∇g ;
for each *pixel in each finite element* **do**
  Step 3: Compute isoparametric element local coordinates ;
  Step 4: Compute isoparametric element $\boldsymbol{\psi}$ matrix ;
  Step 5: Compute isoparametric element Jacobian $\mathbf{J}$ matrix;
  Step 6: Compute spatial gradient of $\boldsymbol{\psi}$ matrix: $D\boldsymbol{\psi}$;
  Step 7: Assemble onto stiffness matrix $\mathbf{M} = \mathbf{M} + [\boldsymbol{\psi}^T \nabla g][\boldsymbol{\psi}^T \nabla g]^T$ using (13);
  Step 8: (Optional) Add regularizer term onto stiffness matrix, e.g. $\alpha[D\boldsymbol{\psi}]^T[D\boldsymbol{\psi}]$
end
while $\|\delta\mathbf{u}\| > \varepsilon$ **do**
  Step 9: Warp deformed image g with current displacement $\mathbf{u}_n$;
  Step 10: Assemble vector $\mathbf{b}$ using (14);
  Step 11: Add regularizer term onto vector $\mathbf{b}$ if **Step 8** has been done ;
  Step 12: Solve $\delta\mathbf{u}$ by (12) ;
  Step 13: Update displacement $\mathbf{u}_{k+1} = \mathbf{u}_k + \delta\mathbf{u}$
end

Augmented Lagrangian DIC (ALDIC) Method

We now introduce a new image comparision algorithm, augmented Lagrangian DIC (ALDIC), that seeks to combine the advantages of both the local subset DIC (speed and parallel implementation) and the global DIC (displacement compatibility and strain smoothness).

Formulation

Recall the ansatz (5) we make in local subset DIC. In this ansatz, the local displacement $\mathbf{u}_i$ and local displacement gradient $\mathbf{F_i}$ in the subdomain Ω_i are independent of each other, and independent for each i. Thus, there is no guarantee of compatibility for the deformation. However, if the displacement field were compatible, then the displacements and the displacement gradients would not be independent, but instead satisfy a global constraint

$$\{\mathbf{F}\} = \mathbf{D}\{\mathbf{u}\} \tag{15}$$

where $\mathbf{D}$ is the discrete gradient operator that depends on the discretization (see Appendix B for an example of first order finite differences). The local subset DIC ignores this constraint while the global DIC enforces this constraint by kinematic construction.

The key idea of ALDIC is to treat this constraint (15) efficiently. We do so by leaving $\mathbf{F}_i$ and $\mathbf{u}_i$ discrete as before, and introduce an auxiliary compatible displacement field $\hat{\mathbf{u}}$ such that

$$\mathbf{F}_i = \nabla\hat{\mathbf{u}}(\mathbf{X}_{i0}), \quad \mathbf{u}_i = \hat{\mathbf{u}}(\mathbf{X}_{i0}). \tag{16}$$

In other words, we minimize (2) subject to the ansatz (5) and constraints (16). We do so using an augmented Langrangian method. Specifically, we consider the correlation functional

$$\begin{aligned}\mathcal{L}_0 = \sum_i \int_{\Omega_i} \big(&|f(\mathbf{X}) - g(\mathbf{X}+\mathbf{u}_i+(\mathbf{F}_i(\mathbf{X}-\mathbf{X}_{i0})))|^2 \\ &+\tfrac{\beta}{2}\left|(\mathbf{D}\hat{\mathbf{u}})_i - \mathbf{F}_i\right|^2 + \boldsymbol{\nu}_i : ((\mathbf{D}\hat{\mathbf{u}})_i - \mathbf{F}_i) + \tfrac{\mu}{2}\left|\hat{\mathbf{u}}_i - \mathbf{u}_i\right|^2 + \boldsymbol{\lambda}_i \cdot ((\hat{\mathbf{u}})_i - \mathbf{u}_i)\big)\, d\mathbf{X}\end{aligned} \tag{17}$$

where we use the matrix or Frobenius norm for matrices $|\mathbf{A}|^2 = \sum_{ij}|a_{ij}|^2$, vector norm for vectors $|\mathbf{a}|^2 = \sum_i a_i^2$, and : for double dot product between two matrices $\mathbf{A} : \mathbf{B} = \sum_{ij} A_{ij}B_{ij}$. Above, $\{\boldsymbol{\nu}_i\}$, $\{\boldsymbol{\lambda}_i\}$ are Lagrange multipliers that enforce the constraints (16). Finally, β and μ are two positive real scalers. If $\beta = \mu = 0$, then this functional gives the traditional Lagrange multiplier formulation if we change the sign of $\{\boldsymbol{\nu}_i\}$, $\{\boldsymbol{\lambda}_i\}$. On the other hand if β and μ were very large with $\boldsymbol{\nu}_i = \boldsymbol{\lambda}_i = \mathbf{0}$, then we have a penalty method. Choosing β and μ to be positive real scalars while retaining the Lagrange multipliers is referred to as the augmented Lagrangian method, and gives rise to well-conditioned numerical problems [38].

Given β and μ, we iteratively minimize $\mathcal{L}_0$ over $\{\mathbf{F}_i\}$, $\{\mathbf{u}_i\}$ and $\{\hat{\mathbf{u}}_i\}$ and update $\{\boldsymbol{\nu}_i\}$ and $\{\boldsymbol{\lambda}_i\}$. Before we proceed, it is convenient to make the following modication to the functional above. We set $\mathbf{W}_i := \boldsymbol{\nu}_i/\beta$, $\mathbf{v}_i := \boldsymbol{\lambda}_i/\mu$ and define

$$\begin{aligned}\mathcal{L} = \sum_i \int_{\Omega_i} \big(&|f(\mathbf{X}) - g(\mathbf{X}+\mathbf{u}_i+(\mathbf{F}_i(\mathbf{X}-\mathbf{X}_{i0})))|^2 \\ &+\tfrac{\beta}{2}\left|(\mathbf{D}\hat{\mathbf{u}})_i - \mathbf{F}_i + \mathbf{W}_i\right|^2 + \tfrac{\mu}{2}\left|\hat{\mathbf{u}}_i - \mathbf{u}_i + \mathbf{v}_i\right|^2\big)\, d\mathbf{X}.\end{aligned} \tag{18}$$

Notice that minimizing $\mathcal{L}_0$ over $\{\mathbf{F}_i\}$, $\{\mathbf{u}_i\}$ and $\{\hat{\mathbf{u}}_i\}$ is the same as minimizing over $\mathcal{L}$ since they differ by quadratic terms independent of $\{\mathbf{F}_i\}$, $\{\mathbf{u}_i\}$ and $\{\hat{\mathbf{u}}_i\}$.

We solve this problem using an alternating direction method of multipliers that allows us to break it up into simpler problems.

Alternating Direction Method of Multipliers

We use alternating direction method of multipliers (ADMM) where local subproblems are coordinated to find a solution to a large global problem [44] to iteratively solve the problem.

Given $\{\mathbf{F}_i^k\}$, $\{\mathbf{u}_i^k\}$, $\{\hat{\mathbf{u}}_i^k\}$, $\{\mathbf{W}_i^k\}$, $\{\mathbf{v}_i^k\}$, we find the $(k+1)$th update as follows:

- Subproblem 1: local update. While holding $\{\hat{\mathbf{u}}_i^k\}$, $\{\mathbf{W}_i^k\}$, $\{\mathbf{v}_i^k\}$ fixed, minimize $\mathcal{L}$ over $\{\mathbf{F}_i\}$, $\{\mathbf{u}_i\}$, to obtain $\{\mathbf{F}_i^{k+1}\}$, $\{\mathbf{u}_i^{k+1}\}$:

$$\{\mathbf{F}_i^{k+1}\}, \{\mathbf{u}_i^{k+1}\} = \underset{\{\mathbf{F}_i\},\{\mathbf{u}_i\}}{\arg\min}\, \mathcal{L}\left(\{\mathbf{F}_i\}, \{\mathbf{u}_i\}, \{\hat{\mathbf{u}}_i^k\}, \{\mathbf{W}_i^k\}, \{\mathbf{v}_i^k\}\right). \tag{19}$$

  Since $\{\hat{\mathbf{u}}_i^k\}$ and hence $\{(\mathbf{D}\hat{\mathbf{u}})_i^k\}$ are known, this problem breaks into a series of local problems that can be solved independently for each i:

$$\begin{aligned}\mathbf{F}_i^{k+1}, \mathbf{u}_i^{k+1} = \underset{\mathbf{F}_i,\mathbf{u}_i}{\arg\min}\, \mathcal{L}_i = \underset{\mathbf{F}_i,\mathbf{u}_i}{\arg\min} \int_{\Omega_i} \big(&|f(\mathbf{X}) - g(\mathbf{X}+\mathbf{u}_i+(\mathbf{F}_i(\mathbf{X}-\mathbf{X}_{i0})))|^2 \\ &+\tfrac{\beta}{2}\left|(\mathbf{D}\hat{\mathbf{u}})_i^k - \mathbf{F}_i + \mathbf{W}_i^k\right|^2 + \tfrac{\mu}{2}\left|\hat{\mathbf{u}}_i^k - \mathbf{u}_i + \mathbf{v}_i^k\right|^2\big)\, d\mathbf{X}.\end{aligned} \tag{20}$$

This is similar to local subset DIC and can be solved by any of the methods described in "Local Subset DIC Method".

- Subproblem 2: global update. While holding $\{\mathbf{F}_i^{k+1}\}, \{\mathbf{u}_i^{k+1}\}, \{\mathbf{W}_i^k\}, \{\mathbf{v}_i^k\}$ fixed, we minimize $\mathcal{L}$ over $\{\hat{\mathbf{u}}_i\}$ to obtain $\{\hat{\mathbf{u}}_i^{k+1}\}$:

$$\begin{aligned}\{\hat{\mathbf{u}}_i^{k+1}\} &= \arg\min_{\{\hat{\mathbf{u}}_i\}} \mathcal{L}\left(\{\mathbf{F}_i^{k+1}\}, \{\mathbf{u}_i^{k+1}\}, \{\hat{\mathbf{u}}_i\}, \{\mathbf{W}_i^k\}, \{\mathbf{v}_i^k\}\right) \\ &= \arg\min_{\{\hat{\mathbf{u}}_i\}} \sum_i \int_{\Omega_i} \left(\frac{\beta}{2}\left|(\mathbf{D}\hat{\mathbf{u}})_i - \mathbf{F}_i^{k+1} + \mathbf{W}_i^k\right|^2 + \frac{\mu}{2}\left|\hat{\mathbf{u}}_i - \mathbf{u}_i^{k+1} + \mathbf{v}_i^k\right|^2\right) d\mathbf{X}.\end{aligned} \tag{21}$$

Note that this is a global problem, but is independent of the images f, g. Indeed, it leads to the linear problem

$$\left(\beta\mathbf{D}^T\mathbf{D} + \mu\mathbf{I}\right)\hat{\mathbf{u}}^{k+1} = \left(\beta\mathbf{D}^T\mathbf{a} + \mu\mathbf{b}\right) \tag{22}$$

where $\mathbf{a} = \{\mathbf{F}_i^{k+1} - \mathbf{W}_i^k\}$ and $\mathbf{b} = \{\mathbf{u}_i^{k+1} - \mathbf{v}_i^k\}$. The solution is given by

$$\hat{\mathbf{u}}^{k+1} = \left(\beta\mathbf{D}^T\mathbf{D} + \mu\mathbf{I}\right)^{-1}\left(\beta\mathbf{D}^T\mathbf{a} + \mu\mathbf{b}\right). \tag{23}$$

Since β and μ are fixed, the matrix $\left(\beta\mathbf{D}^T\mathbf{D} + \mu\mathbf{I}\right)^{-1}$ can be precomputed and stored, and therefore this step becomes a simple matrix-vector multiplication. Further, the matrix $\mathbf{D}$ has a structure, and therefore this matrix-vector multiplication can be carried out very efficiently.

- Subproblem 3: Lagrange multiplier update. We finally update $\{\mathbf{W}_i\}, \{\mathbf{v}_i\}$ as follows:

$$\mathbf{W}_i^{k+1} = \mathbf{W}_i^k + \left((\mathbf{D}\hat{\mathbf{u}})_i^{k+1} - \mathbf{F}_i^{k+1}\right), \tag{24}$$

$$\mathbf{v}^{k+1} = \mathbf{v}^k + \left(\hat{\mathbf{u}}^{k+1} - \mathbf{u}^{k+1}\right). \tag{25}$$

- Stopping criterion. Theoretically, we should check the convergence of all quantities during ALDIC iterations. However, in practice, we care most about the displacements. Therefore, we simply check $\left(\hat{\mathbf{u}}^{k+1} - \hat{\mathbf{u}}^k\right)$, and stop if this happens to be smaller than a given tolerance.

Convergence

We briefly recall some results from Boyd et al. [44] that apply to the ADMM alogrithm proposed above. Assume that the following conditions are true:

- Assumption 1. The functional C_i in Eq. 7 or the first term of $\mathcal{L}$ can be approximated by a closed, proper, and convex functional near the optimal solution.
- Assumption 2. The Lagrangian $\mathcal{L}_0$ with $\beta = \mu = 0$ has a saddle point; i.e., there exist $(\{\mathbf{F}_i^*\}, \{\mathbf{u}_i^*\}, \{\hat{\mathbf{u}}_i^*\}, \{\boldsymbol{\nu}_i^*\}, \{\boldsymbol{\lambda}_i^*\})$, for which

$$\begin{aligned}\mathcal{L}_0(\{\mathbf{F}_i^*\}, \{\mathbf{u}_i^*\}, \{\hat{\mathbf{u}}_i^*\}, \{\boldsymbol{\nu}_i\}, \{\boldsymbol{\lambda}_i\}) &\le \mathcal{L}_0(\{\mathbf{F}_i^*\}, \{\mathbf{u}_i^*\}, \{\hat{\mathbf{u}}_i^*\}, \{\boldsymbol{\nu}_i^*\}, \{\boldsymbol{\lambda}_i^*\}) \\ &\le \mathcal{L}_0(\{\mathbf{F}_i\}, \{\mathbf{u}_i\}, \{\hat{\mathbf{u}}_i\}, \{\boldsymbol{\nu}_i^*\}, \{\boldsymbol{\lambda}_i^*\})\end{aligned}$$

for all $(\{\mathbf{F}_i\}, \{\mathbf{u}_i\}, \{\hat{\mathbf{u}}_i\}, \{\boldsymbol{\nu}_i\}, \{\boldsymbol{\lambda}_i\})$.

Then, we have the following convergence

- Primal residual convergence. $\left(\mathbf{D}\hat{\mathbf{u}}^k - \mathbf{F}^k\right) \to 0$ and $\left(\hat{\mathbf{u}}^k - \mathbf{u}^k\right) \to 0$ as $k \to \infty$, i.e., the constraints are satisfied asymptotically;
- Dual residual convergence. $\left(\hat{\mathbf{u}}^{k+1} - \hat{\mathbf{u}}^k\right) \to 0$ as $k \to \infty$, i.e., the dual feasibility is satisfied asymptotically, see Appendix C;
- Objective convergence. $\mathcal{L}^k \to \mathcal{L}^*$ as $k \to \infty$, i.e., the Lagrangian approaches its optimal value;
- Dual variable convergence. $\mathbf{W}^k \to \mathbf{W}^*, \mathbf{v}^k \to \mathbf{v}^*$ as $k \to \infty$, where $(\mathbf{W}^*, \mathbf{v}^*)$ is dual optimal point.

Note that the local functional C_i can be highly oscillatory and is thus not convex. However, if the initial guess for the local variables $(\{\mathbf{F}_i\}, \{\mathbf{u}_i\})$ is in the convergence basin of local subset DIC, then the first assumption is true. If this assumption is false, then subproblem 1 (19) above diverges; this provides a check that this assumption holds.

A Simplification and ALDIC Algorithm

We now make one final simplification to subproblem 1 to speed up ALDIC algorithm. The local problem (20) requires us to minimize over both $\mathbf{u}_i$ and $\mathbf{F}_i$: this makes the local problem large and the overall convergence slow. Further, the high dimensionality can lead to local minima and thus poor accuracy. This is consistent with the practice of using only the displacements in most commonly used local subset DIC. Therefore, we simplify the ALDIC subproblem 1 as follows: in the $k+1$ iteration step, we update $\mathbf{F}^{k+1}$ to be exactly equal to $\mathbf{D}\hat{\mathbf{u}}^k$ and only solve for $\mathbf{u}^{k+1}$. We still use the same IC-GN iteration method as introduced in previous "Local Subset DIC Method" local subset DIC.

The overall algorithm is given in Algorithm 3.

Demonstration

We now demonstrate the ALDIC method, and compare it to both local subset DIC and global DIC methods. All algorithms are implemented in Matlab. We use the following parameters unless it is specified otherwise. We use

Table 1 List of symbols used in the demonstration section

$\mathbf{F}^k$	Solved deformation gradient tensor in the k-th ADMM iteration Subproblem 1
$\mathbf{u}^k$	Solved displacement vector in the k-th ADMM iteration Subproblem 1
$\mathbf{u}^k$	Solved displacement vector in the k-th ADMM iteration Subproblem 2
$\mathbf{W}^k$, $\mathbf{v}^k$	Dual variables in the k-th ADMM iteration
u,	x-direction displacement component
v,	y-direction displacement component
e_{xx}, e_{yy}, e_{xy}	The "xx","yy" and "xy" components of infinitesimal strain

bi-cubic interpolations for the grayscale value at subpixel positions. In the local subset DIC, we stop IC-GN iterations when $\|d_i\|$, $\|e_{jk}\| < 10^{-6}$. Usually the IC-GN reaches convergence point within several iteration steps. In the global DIC, we use Q4 finite element with a bilinear form of the domain's displacement field trying to approximate the exact nonuniform one. We stop the iteration when the average magnitude of the nodal displacement update is smaller than 10^{-6} pixels. In ALDIC, we start $\mathbf{W}$ and $\mathbf{v}$ from zero. We choose μ to be $O(10^{-3}) \sim O(10^{-1})$ times diagonal terms of a'_{ip}. We take $\beta = \left[O(10^{-1}) \sim O(10^{0}) \cdot \text{element size}^2 \cdot \mu\right]$ to balance the relevant terms. We use the same stop criteria in subproblem 1 as local subset DIC ($\|d'_i\|_{L_2} < 10^{-6}$), and the whole ALDIC iteration stops when $\|\hat{\mathbf{u}}^{k+1} - \hat{\mathbf{u}}^k\|_{L_2} < 10^{-4}$.

Algorithm 3 ALDIC

Input: Reference image f, deformed image g
Output: Displacement $\mathbf{u}_i$, deformation gradient tensor $\mathbf{F}_i$ of each local subset, global displacement $\hat{\mathbf{u}}$
Step 1: Initialization using FFT integer pixel search method;
Step 2: Precompute finite difference operator $\mathbf{D}$;
Step 3: Choose initial parameters β, μ. Set dual variables $\mathbf{W}$, $\mathbf{v}$ to be zero;
while $\|\hat{\mathbf{u}}^{k+1} - \hat{\mathbf{u}}^k\| > \varepsilon$ **do**
  Step 4: Solve subproblem 1 (20) as in Algorithm 1 for $\mathbf{u}^{k+1}$, $\mathbf{F}^{k+1}$,;
  Step 5: Solve subproblem 2 (23) for $\hat{\mathbf{u}}^{k+1}$;
  Step 6: Update dual variables $\mathbf{W}$, $\mathbf{v}$ by (24), (25)
end

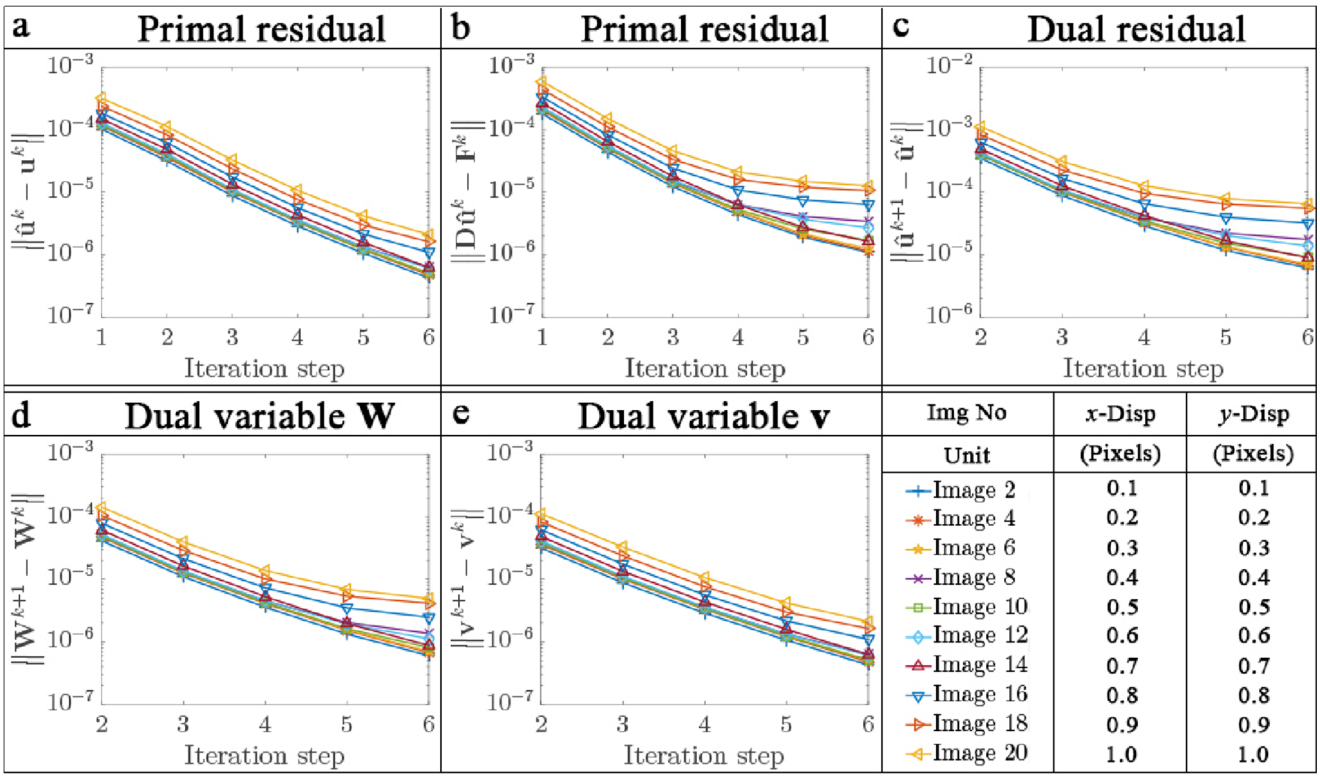

Fig. 3 Convergence of the ALDIC method for the SEM 2D-DIC synthetic images, sample 1 representing translation

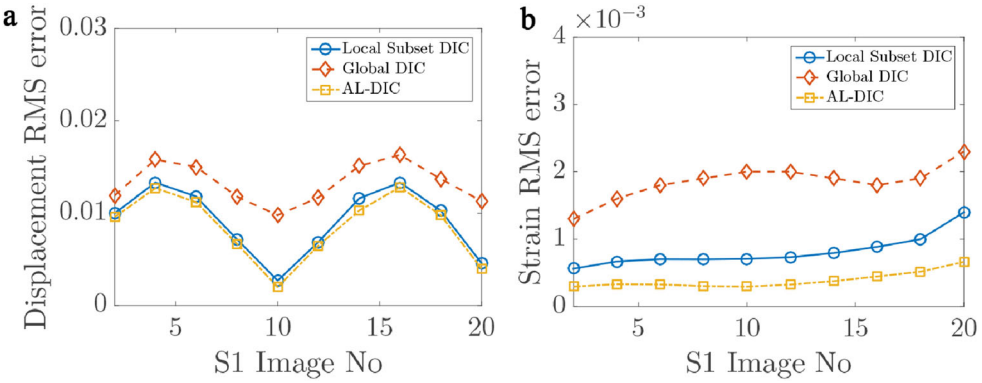

Fig. 4 Comparison of RMS error in displacement (**a**) and strain (**b**) computed with the three methods for the synthetic images in the SEM 2D-DIC, sample 1 or translation

When studying synthetic images where the exact deformation is known, we use the root-mean-square (RMS) error,

$$\text{RMS error} := \sqrt{\frac{\sum_{\#\text{ of nodes}} |\text{Numerical result} - \text{Exact value}|^2}{\#\text{ of nodes}}} \tag{26}$$

in both the displacement and strain. RMS error reflects globally how far the computed results are away from the exact values and is a measure of the standard variance of the computation error.

In local subset DIC, we report the deformation gradients/strains obtained directly by the local subset DIC correlation. In global DIC, we compute nodal strains by extrapolating the strains from the finite element Gauss points. In ALDIC, the strain field is obtained directly from $\mathbf{D}\hat{\mathbf{u}}$. We summarize the symbols we used in the demonstration section in Table 1.

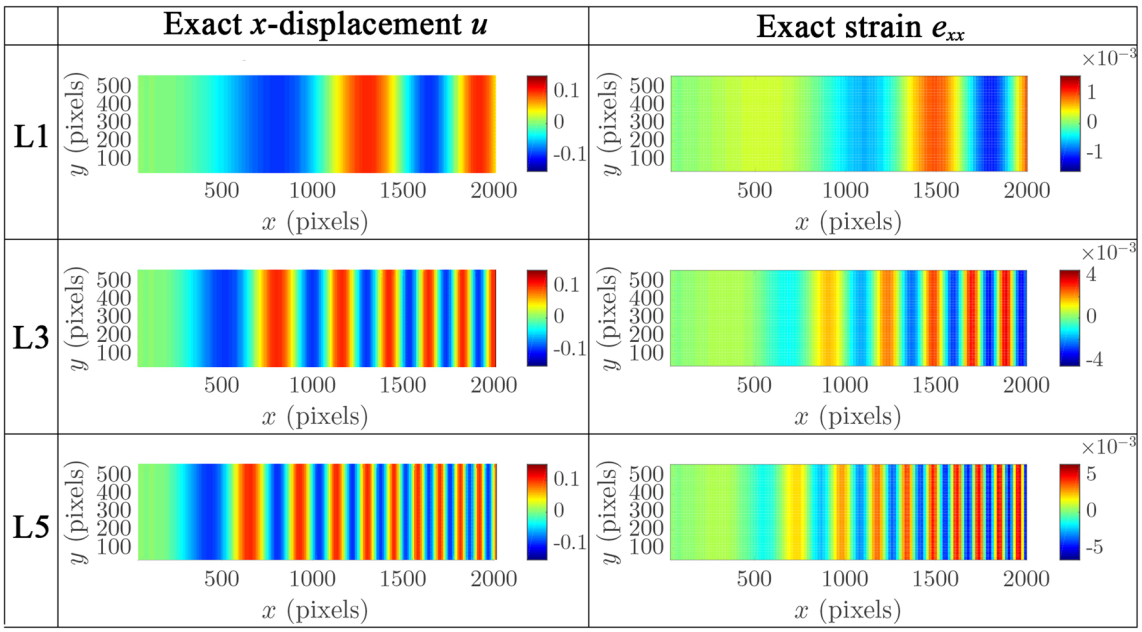

Fig. 5 Exact horizontal x-displacement and strain e_{xx} field associated with Sample 14 images L1, L3 and L5

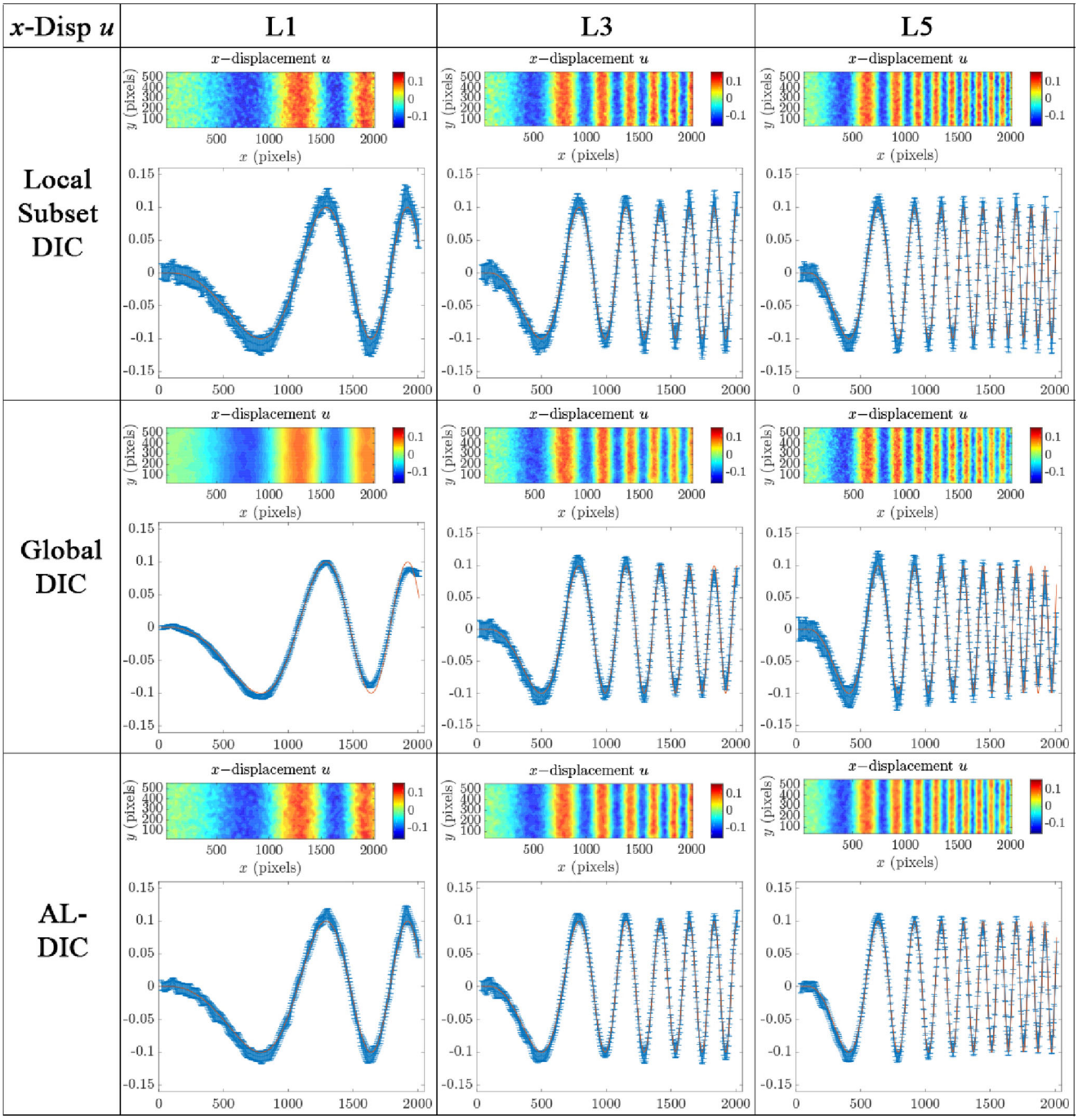

Fig. 6 The horizontal displacement (u) obtained using the three methods from the synthetic images of SEM 2D-DIC sample 14: L1, L3, L5

Case Study I: Synthetic Images from the SEM 2D-DIC Challenge

We study synthetic images from the SEM 2D-DIC challenge, samples 1 & 14 [52].[1] Sample 1 represents a series of pure translations while sample 14 represents a sinusoidal deformation with changing frequency.

Translation: Sample 1

The deformations in Sample 1 are pure translations in both x and y directions with amplitudes ranging from 0 to 1 pixel

[1] https://sem.org/dic-challenge/2d-test-image-sets.asp

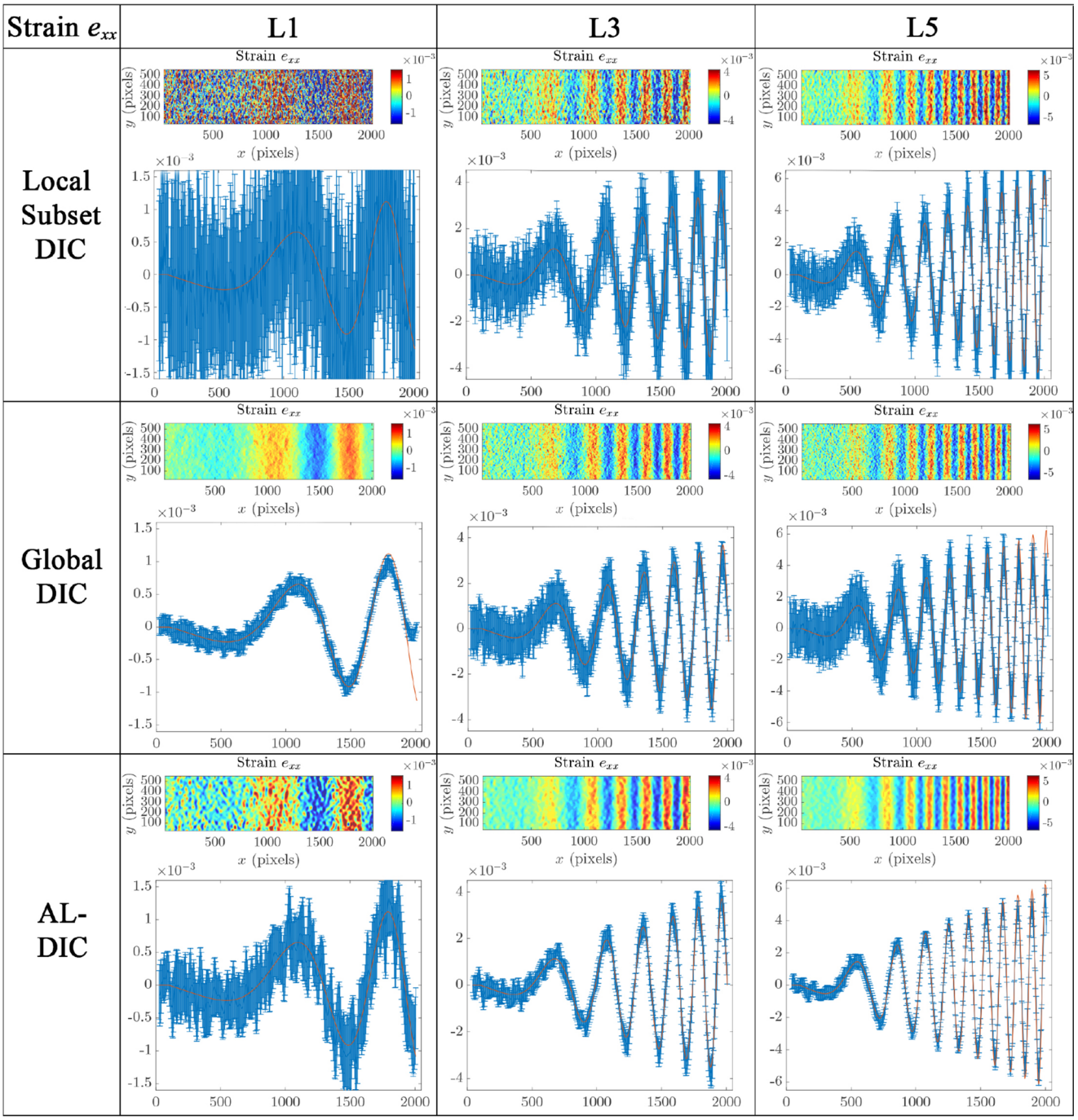

Fig. 7 The horizontal longitudinal strain (e_{xx}) obtained using the three methods from the synthetic images of SEM 2D-DIC sample 14: L1, L3, L5

in increments of 0.1 pixels. We set all the local window sizes to be 20×20 pixels, and set both the local neighboring windows distance and global element size to be 5×5 pixels.

Figure 3 shows the convergence of the various quantities (without a stopping criterion). We see that ALDIC behaves well and converges within 6 steps. Figure 4 shows the RMS errors in displacements and strains, and compares with the corresponding errors in the local subset DIC and global DIC methods. We observe that ALDIC has the smallest errors in all cases.

We make a couple of comments. First, we see that the error of the global DIC method is high in this case. This is

Table 2 Comparison of the RMS errors in displacement and strain for the SEM 2D-DIC synthetic images of sample 14: L1,L3,L5

	Image	Local subset	Regularized	ALDIC
	No	DIC	global DIC	
x displacement (pixels)	L1	0.0212	0.0234	0.0141
	L3	0.0202	0.0162	0.0136
	L5	0.0201	0.0080	0.0139
Strain e_{xx}	L1	3.18×10^{-3}	3.15×10^{-4}	1.00×10^{-3}
	L3	3.19×10^{-3}	1.90×10^{-3}	9.84×10^{-4}
	L5	3.20×10^{-3}	3.15×10^{-3}	9.83×10^{-4}

because we do not use a regularization since a regularizer forces zero gradient which artificially forces the desired answer. Second, when using synthetic images, a bias can be introduced if the interpolation used for subpixel shifting is different from those used for creating the images. The sinusoidal variation with image number is a reflection of this bias. We use a bi-cubic interpolation in our work based on the study of Bornert et al. [53].

Heterogeneous Deformation: Sample 14

The deformations in Sample 14 are sinusoidal with varying frequency in the x direction as shown in Fig. 5 for the three images – L1, L3, and L5 – that we use. It has zero displacement in the y direction. We set all the local window sizes to be 30×30 pixels, and set both the local neighboring windows distance and global element size to be 5×5 pixels. As before, the ALDIC method converges in about six iterations (we have omitted the figure for brevity). Figures 6 and 7 show the horizontal displacement (u) and the horizontal longitudinal strain (e_{xx}) for the three images and the three methods. These figures show that the ALDIC leads to smooth displacement fields and this is reflected in the strain. Table 2 shows the RMS errors for strain and displacement, and shows that the ALDIC method leads to smaller errors compared to the other two methods.

We also use the image L1 from this set to study the effect of the subset size in the ALDIC method. Table 3 shows the RMS errors in displacement and strain using three window sizes. Not surprisingly, the errors increase with decreasing window size.

Case Study II: Experimental Heterogeneous Fracture Deformation

We conclude our case studies by analyzing data from an experiment on the fracture of a heterogeneous material taken from Avellar [54]. The $50.8 \times 45.7 \times 9.5$ mm specimen that is shown in Fig. 8(a) is 3D printed using a compliant material (Stratasys proprietary acrylic DM9895, E=45 MPa) shown in dark and a stiff material (Stratasys proprietary acrylic RGD835, E=1960 MPa, ν = 0.399) shown in grey. We choose this example because the heterogeneous stiffness leads to complex strain and displacement fields. A speckle pattern is applied using white spray paint and the specimen is loaded using the two pins inserted into the holes and pulled to failure. The reference image and one deformed image of the sample (the area in the red box of Fig. 8(a)) under loading are shown in Fig. 8(b, c), where the length scale in the digital image is 0.037 mm/pixel. We set all the local window sizes to be 16×16 pixels, and set both the local neighboring windows

Table 3 DIC displacement and strain RMS errors of Sample 14 L1 with different window sizes

	Subset	Local subset	Regularized	ALDIC
	Size	DIC	global DIC	
x displacement (pixels)	30×30	0.0199	0.0079	0.0056
	20×20	0.0323	0.0082	0.0067
	10×10	0.0990	0.0088	0.0165
Strain e_{xx}	30×30	3.30×10^{-3}	2.08×10^{-4}	9.57×10^{-5}
	20×20	7.78×10^{-3}	2.35×10^{-4}	1.62×10^{-4}
	10×10	9.90×10^{-2}	2.84×10^{-4}	8.19×10^{-4}

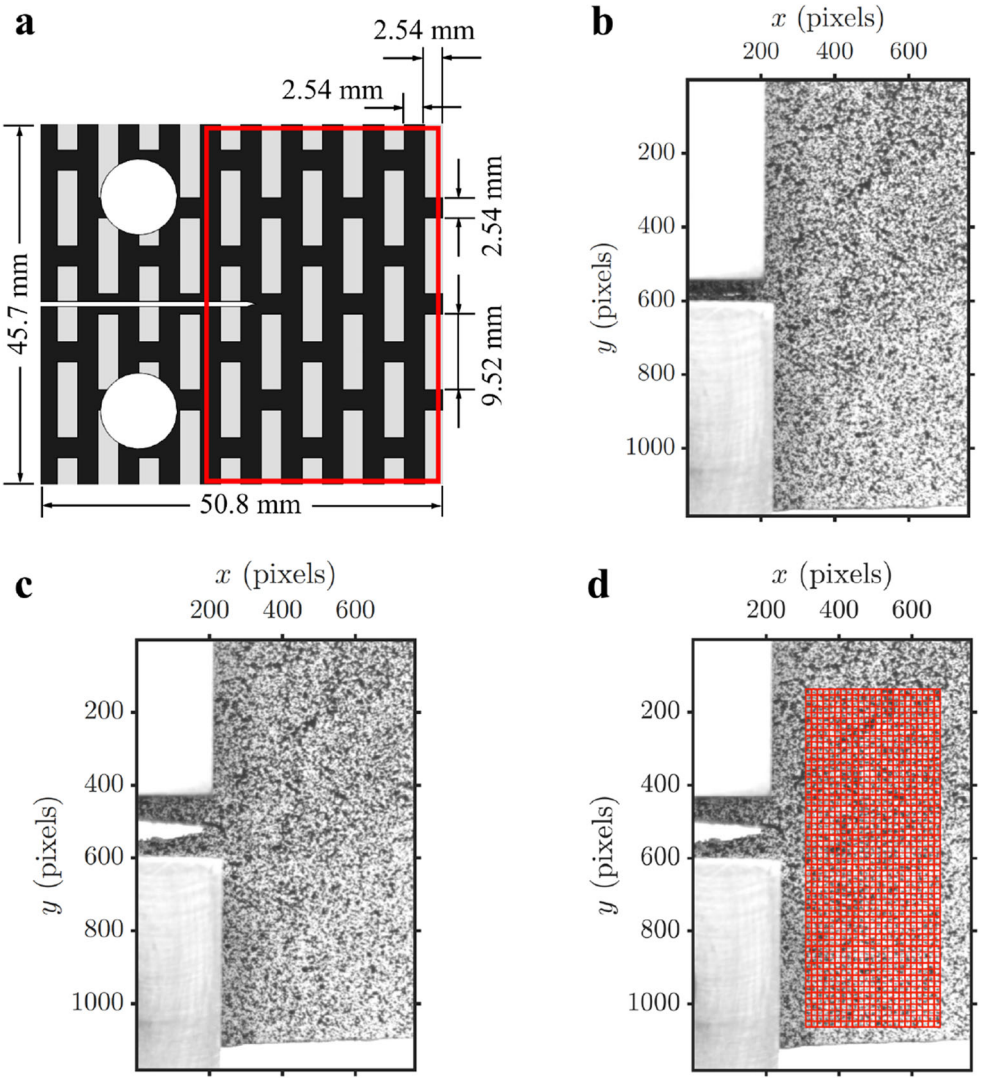

Fig. 8 Heterogeneous specimen used for the third case study. **a** Front view of designed fracture specimen with brick architecture, where the box area will be captured using a CCD camera. **b** A speckle pattern is applied using white spray paint onto the surface of the specimen where the length scale of the digital image is 0.037 mm/pixel. **c** One deformed image of the sample as the crack propogates under loading. **d** The local subsets/global finite element mesh used in all three DIC methods

distance and global element size also to be 16 × 16 pixels, see Fig. 8(d). The resulting images are analyzed using all three DIC methods. The convergence of the ALDIC method is shown in Fig. 9. The displacement and strain fields obtained using all three methods are shown in Fig. 10. We see little difference in the horizontal displacement u, but the vertical displacement v differ in the noise. ALDIC is less noisy than global DIC, which in turn is less noisy than the local subset DIC. This is also reflected in the strain fields.

Computational Cost

We compare the computational cost of the three DIC algorithms. The symbols used are listed in Table 4. We estimate the cost of each step in each algorithm, and these are listed in Tables 5, 6 and 7. We then use the dominant terms (assuming that $k_1 << k_2$) to estimate the total cost, and these are also listed in the tables. We observe that all algorithms, properly implemented, scale linearly with the size of the image mN. Thus, the differences are in the pre-factors, and these can be significant as we presently demonstrate. We also note that the local subset DIC and ALDIC can be easily parallelized.

Table 8 lists the computational clock time for the case studies. All studies are performed on the same workstation with Intel (R) Xeon(R) CPU E5-2650 v3 2.30 GHz (2 Processors), RAM 32.0 GB Memory, 64-bit nodes. In the local subset DIC and ALDIC Subproblem 1 IC-GN iterations, we use 20 clusters and process it in parallel in Matlab. It is clear from the table that local subset DIC is the least expensive, and global DIC is the most expensive as expected.

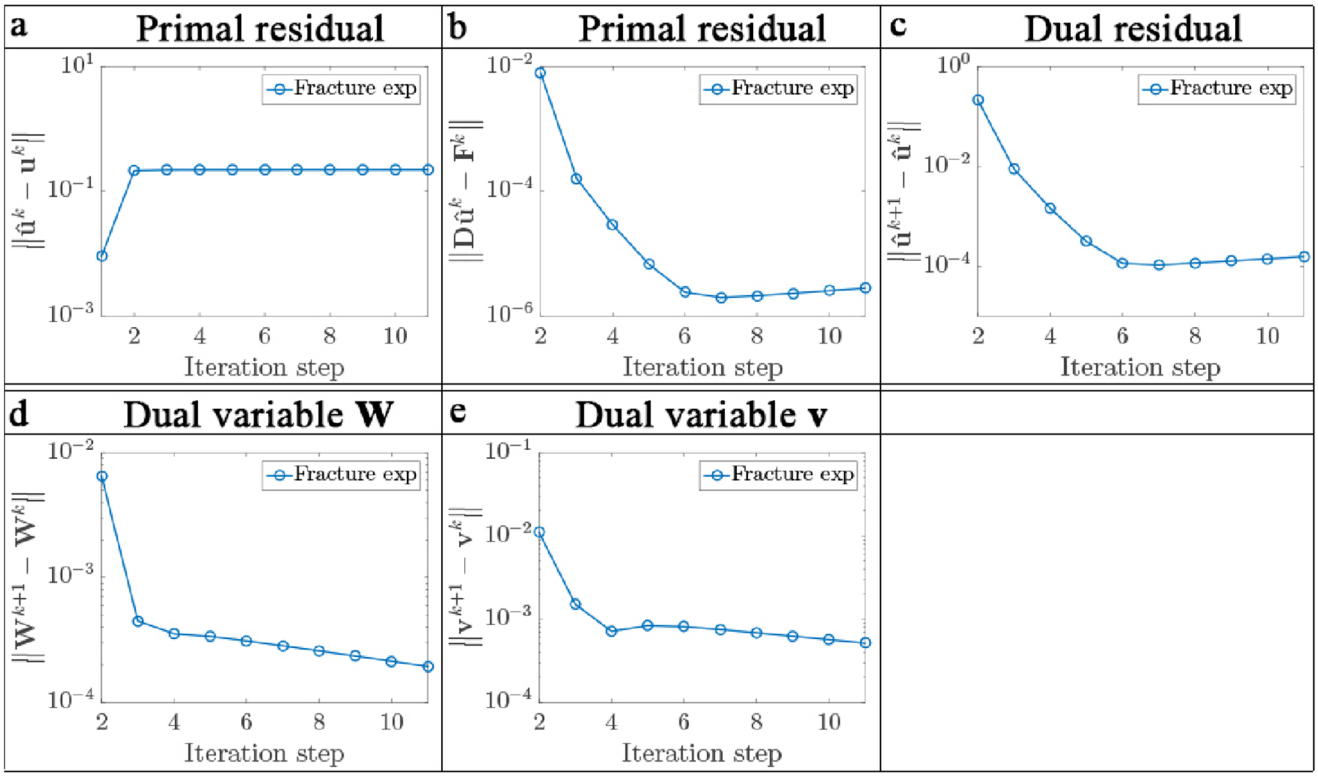

Fig. 9 Convergence of ALDIC method in heterogeneous fracture experiment

Discussion and Conclusion

In this paper, we have presented a new method, the augmented Lagrangian digital image correlation (ALDIC), for image matching. It combines the advantages of the two established methods, the speed of local subset DIC and the kinematic compatibility of global DIC. We show in "Demonstration" through a series of case-studies using synthetic images that ALDIC provides superior accuracy compared to the established methods. We show in "Computational Cost" that the computational cost of ALDIC is only a few times that of local subset DIC and less than that of global DIC.

ALDIC correlates subsets locally to find a displacement field as in local subset DIC, but then ties them together by introducing an auxiliary compatible displacement field. This leads to superior accuracy compared to local subset DIC for two reasons. First, the local correlation or sub-problem 1 has some global information through the augmented Lagrangian and auxiliary field – see (Eq. 20). Second, the auxiliary field leads to less noisy deformation gradients as shown in Fig. 11. However, ALDIC is more expensive than local subset DIC because it requires the solution of a global problem (22). Still, this is not prohibitive: we see in "Computational Cost" that it is only a few times that of local DIC.

Both ALDIC and global DIC seek to impose compatibility. However, the point of departure is that ALDIC does not use a basis set to impose compatibility anywhere, but does so using an augmented Lagrangian. Therefore, the resulting operator ($\beta \mathbf{D}^T \mathbf{D} + \mu \mathbf{I}$) is the sum of the Laplacian and identity. This is universal, i.e., independent of the problem, displacement or image (though the matrix depends on the discretization). The nature of the operator and the universality allows us to either precompute the inverse (as we do here), or us a variety of established efficient methods (see for example [55]). In contrast, the operator M in Eq. 13 depends on the image, and moreover may be poorly conditioned depending on the image. Regularization can help with the conditioning and it is possible to address the computational cost. However, these require sophistication in their implementation and must be adopted to the problem at hand.

We conclude with a few thoughts on advancing this work. First, all the demonstrations in this work are limited to two dimensional images. However, the presentation of the method and algorithm is valid for two and three dimensions (or digital volume correlation, DVC). Second, we use the IC-GN iteration for the local correlation (subproblem 1). This is robust but slow since it involves pixel-wise summation. We can improve this by using phase correlation methods

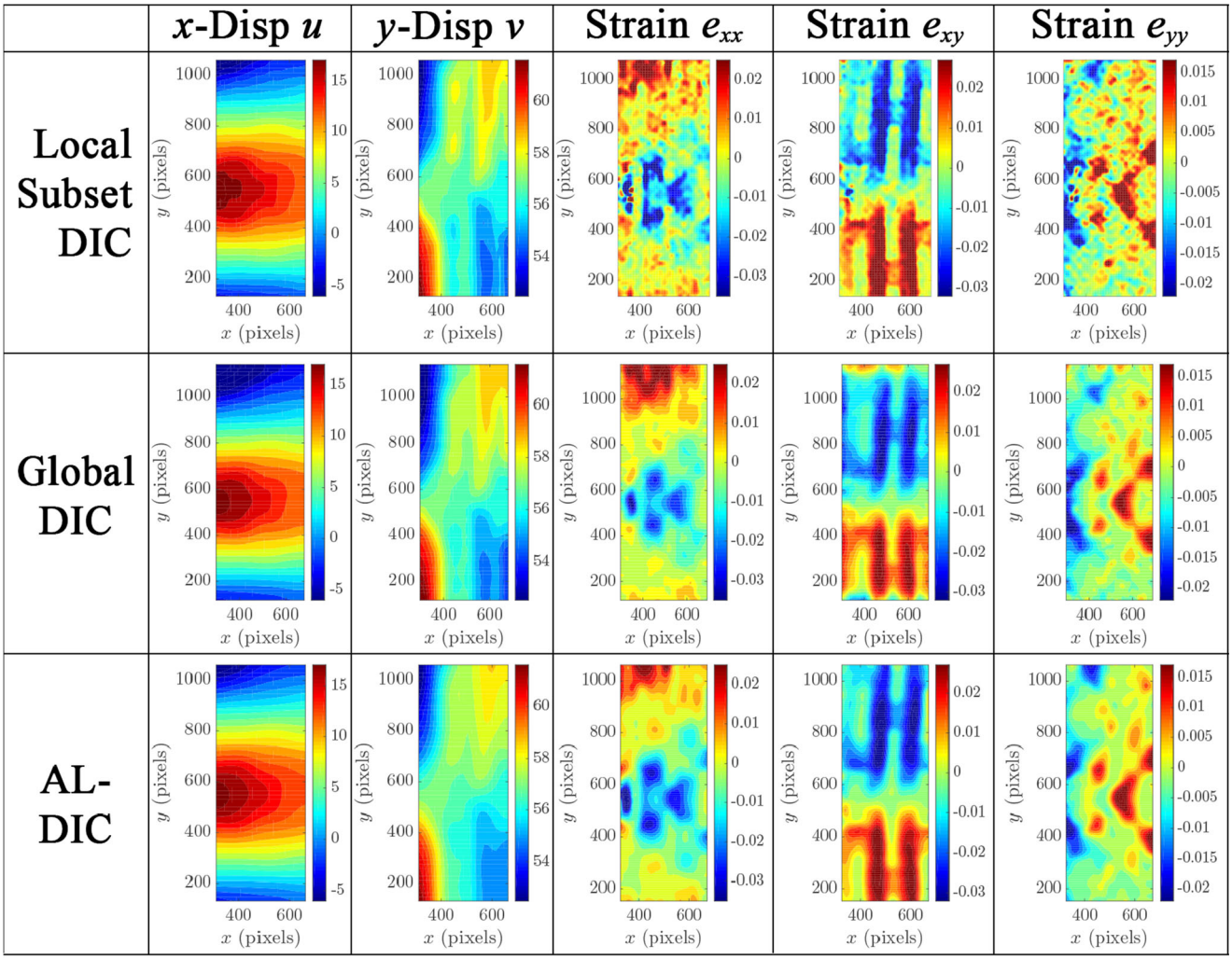

Fig. 10 Contour plot of three DIC algorithms solved displacement and strain fields in heterogeneous fracture experiment

and fast Fourier transforms that have been introduced for local subset DIC. Third, we hold β and μ fixed during ALDIC iterations, but they can also be updated at each iteration step to further speed up iterations, see Ref [44] Section 3.4.1. When varying penalty parameters are used, the scaled dual variables $\mathbf{W} = \boldsymbol{\nu}/\beta$ and $\mathbf{v} = \boldsymbol{\lambda}/\mu$ must also be rescaled after updating parameters β and μ. Fourth, DIC is rather data intensive as it requires

Table 4 List of symbols used in the analysis of computational cost

N	# of pixels in each local subset or each finite element
m	# of total local subsets or finite elements
d	The dimension of images, e.g. $d = 2$ for 2D pixel images
n_L	Length of parameter vectors of each local subset
n_G	Length of parameter vectors in finite element
k_1	Computation cost to compute image grayscale derivatives
k_2	Computation cost to interpolate grayscale value at sub-pixel position
k_3	# of iterations in local subset DIC algorithm
k_4	# of iterations in global DIC algorithm IC-GN scheme
k_5	# of iterations in ALDIC ADMM scheme
k_6	# of inside iterations in ALDIC Subproblem 1 IC-GN scheme
C	# of clusters used in local subset DIC and ALDIC Subproblem 1 for parallel computation

Table 5 The computation cost of the local subset DIC IC-GN iteration

Pre-computation	Step 2	Step 3		
	$O(k_1 dmN)$	$O(n_L{}^2 mN)$		
Per IC-GN iteration	Step 4	Step 5	Step 6	Step 7
	$O(k_2 n_L mN)$	$O(n_L mN)$	$O(n_L{}^3 m)$	$O(n_L{}^3 m)$
Total				$O(k_2 k_3 n_L mN/C)$

Table 6 The computation cost of the global DIC FEM iteration

Pre-computation	Step 2	Step 3	Step 4	Step 5
	$O(k_1 dmN)$	$O(dn_G^3 mN)$	$O(dn_G mN)$	$O(d^2 n_G mN)$
	Step 6	Step 7	Step 8	
	$O(d^6 n_G mN)$	$O(d^4 n_G^2 mN)$	$O(d^4 n_G^2 mN)$	
Per FEM iteration	Step 9	Steps 10-11	Step 12	Step 13
	$O(k_2 dn_G mN)$	$O(d^2 n_G mN)$	$O(dn_G m)$	$O(dn_G m)$
Total				$O(k_2 k_4 d^2 n_G mN)$

Table 7 The computation cost of the ALDIC ADMM iteration

Pre-computation	Steps 2-3		
	$O(2d^2 m)$		
Per ALDIC iteration	Step 4	Step 5	Step 6
	$O(k_2 k_6 n_L mN)$	$O(2d^3 m^2)$	$O(n_L m)$
Total			$O(k_2 k_5 k_6 n_L mN/C)$

Table 8 Computation time using three DIC algorithms

Example Name	Parameter	local subset DIC time cost(s)	Parameter	global DIC time cost(s)	Parameter	Parameter	ALDIC time cost(s)
Theory	k_3	$O(0.3k_3k_2mN)$	k_4	$O(16k_4k_2mN)$	k_5	k_6	$O(0.3k_5k_6k_2mN)$
S14 L1 30 × 30	12.2	28.55	6	478.33	7	6.5	121.63
S14 L1 20 × 20	16.0	37.65	7	630.19	7	7.4	145.95
S14 L1 10 × 10	40.8	95.28	7	1402.3	7	13.3	294.99
S14 L1 5 × 5	12.2	743.36	7	11026	7	6.1	3065.02
S14 L3 5 × 5	12.1	743.36	7	11368	7	6.1	2923.05
S14 L5 5 × 5	12.1	743.36	8	11967	7	6.1	2960.71
Fracture exp	11.6	12.46	8	246.20	7	7.9	52.96
S1 img 2	7.3	46.07	5	338.27	6	2.9	150.25
S1 img 4	6.4	40.78	4	303.01	6	2.5	131.31
S1 img 6	5.9	38.48	4	307.18	6	2.5	127.08
S1 img 8	6.2	40.76	4	305.13	6	2.5	133.19
S1 img 10	6.3	39.95	5	331.99	6	2.6	133.03
S1 img 12	6.2	40.07	4	305.27	6	2.5	132.52
S1 img 14	6.0	38.40	4	304.49	6	2.5	126.21
S1 img 16	6.5	41.51	4	305.07	6	2.6	134.10
S1 img 18	7.4	47.16	5	330.98	6	3.1	156.03
S1 img 20	8.5	52.98	5	335.80	5	3.5	175.51

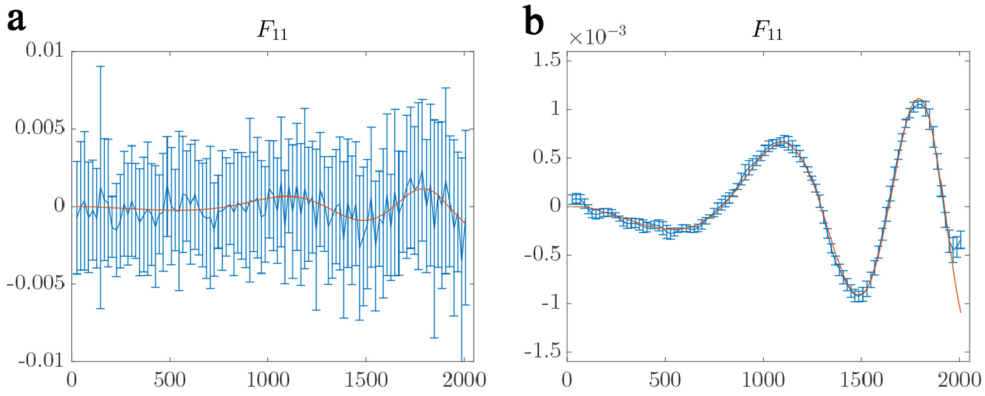

Fig. 11 Comparison of the deformation gradient (F_{11} component) obtained using the local subset DIC (**a**) and ALDIC (**b**) for sample 14 L1

multiple high resolution images. However, the information that we seek is only the displacement and strain fields. Therefore, it would be valuable to combine image matching with image compression so that the amount of data can be significantly reduced without losing any experimental information. We show elsewhere [56] that ALDIC is well suited for this purpose. Finally, in both the local subset DIC and subproblem of ALDIC, the accuracy of displacements increases with subset size. However, the fidelity decreases in regions of large strain or rapidly changing strain. The ideal strategy is to use a multiscale or multigrid approach: large subsets in small strain and small strain-gradient areas, and small subsets in large strain and large strain-gradient areas. We describe this in a forthcoming work [57].

Acknowledgments We are grateful to Dr. Louisa Avellar for sharing her images of heterogeneous fracture with us. We gratefully acknowledge the support of the US Air Force Office of Scientific Research through the MURI grant 'Managing the Mosaic of Microstructure' (FA9550-12-1-0458).

Appendix A: Inverse Compositional Gauss-Newton

In this paper, we use Inverse Compositional Gauss-Newton (IC-GN) scheme to solve local subset DIC optimization. Given the current iterate of deformation map $\mathbf{y}^k$, we seek the

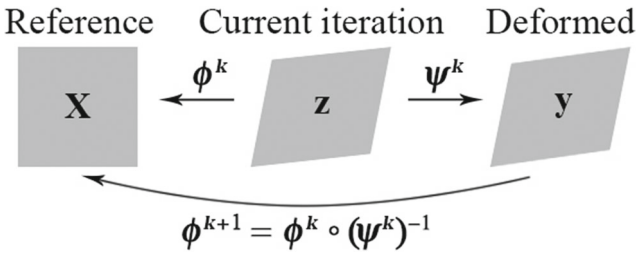

Fig. 12 The change of variables involved in the IC-GN update

updated deformation map $\mathbf{y}^{k+1}$. It is convenient to define the inverse maps $\boldsymbol{\phi}^k$ and $\boldsymbol{\phi}^{k+1}$, where $\boldsymbol{\phi}^k(\mathbf{y}^k(\mathbf{X})) = \mathbf{X}$. We define the increment $\boldsymbol{\psi}^k$ through $\mathbf{y}^{k+1} = (\psi)^k \circ \mathbf{y}^k$ as shown in Fig. 12. We make a change of configuration and rewrite as

$$C_i = \int_{\Omega_i^k} |f(\boldsymbol{\phi}^k(\mathbf{z})) - g(\boldsymbol{\psi}(\mathbf{z}))|^2 d\mathbf{z}, \tag{27}$$

where $\mathbf{z}$ is the current iterate of deformation map $\mathbf{y}^k$. We obtain $\boldsymbol{\psi}^k$ as the minimizer of this functional and the updated deformation map as

$$\phi^{k+1} = \phi^k \circ (\boldsymbol{\psi}^k)^{-1}. \tag{28}$$

To minimize (27), we assume $\boldsymbol{\psi}^k \approx \mathbf{z} + \mathbf{v} + \mathbf{H}(\mathbf{z} - \mathbf{z}_0)$ for small $\mathbf{v}$ and $\mathbf{H}$. Therefore,

$$C_i = \int_{\Omega_i^k} |f(\phi^k(\mathbf{z})) - g(\mathbf{z}) - \nabla g(\mathbf{z}) \cdot (\mathbf{v} + \mathbf{H}(\mathbf{z} - \mathbf{z}_0))|^2 d\mathbf{z}. \tag{29}$$

Minimizing over $\mathbf{v}$ and $\mathbf{H}$, we obtain

$$\begin{pmatrix} a_{lp} & b_{lqr} \\ b_{mnp} & c_{mnqr} \end{pmatrix} \begin{pmatrix} v_p \\ H_{qr} \end{pmatrix} = \begin{pmatrix} d_l \\ e_{mn} \end{pmatrix} \tag{30}$$

where

$$a_{lp} = 2 \int_{\Omega_i^k} g_{,l} g_{,p} d\mathbf{z}, \tag{31}$$

$$b_{lqr} = \int_{\Omega_i^k} g_{,l} g_{,q} (z_r - z_{0r}) d\mathbf{z}, \tag{32}$$

$$c_{mnqr} = 2 \int_{\Omega_i^k} g_{,m} (z_n - z_{0n}) g_{,q} (z_r - z_{0r}) d\mathbf{z}, \tag{33}$$

$$d_l = \int_{\Omega_i^k} (f - g) g_{,l} d\mathbf{z}, \tag{34}$$

$$e_{mn} = \int_{\Omega_i^k} (f - g) g_{,m} (z_n - z_{0n}) d\mathbf{z} \tag{35}$$

and $g_{,l} = \frac{\partial g}{\partial z_l}$ etc. We solve (30) for $\mathbf{v}, \mathbf{H}$ to obtain $\boldsymbol{\psi}^k$. We then obtain the new (inverse) deformation $\boldsymbol{\phi}^{k+1}$ using Eq. 28. In practice, we don't need to compute Ω_i^k

domain at each iteration, instead we directly compute all the integrations (or discrete summations) over the final deformed configuration, which also gives us good results and saves lots of computation time.

We also use IC-GN to solve subproblem 1 or Eq. 20 in ALDIC. This reduces to Eq. 30 above with a_{lp} and d_l replaced with

$$a'_{lp} = 2\int_{\Omega_i^k}(g_{,l}g_{,p} + \frac{\mu}{2}\delta_{lp})d\mathbf{z}, \tag{36}$$

$$d'_l = \int_{\Omega_i^k}((f-g)g_{,l} + \frac{\mu}{2}(u_l - v_l^k - \hat{u}_l^k))d\mathbf{z}. \tag{37}$$

Appendix B: The operator D

The matrix $\mathbf{D}$ in "Augmented Lagrangian DIC (ALDIC) Method" is the discrete gradient operator. This depends on the choice of discretization. In this paper, we use first order finite difference based on an uniform square mesh. We provide explicit details for this case, but note that ALDIC is compatible with any discretization and these would lead to different matrices.

We describe it in one dimension for convenience, and the generalization to higher dimensions is obvious. We assume that the domain is discretized uniformly with the distance h between nodes $x_i, x_2 \ldots x_N$. Then the (15) is explicitly written as

$$\underbrace{\begin{Bmatrix}\mathbf{F}_1\\ \mathbf{F}_2\\ \mathbf{F}_3\\ \vdots\\ \mathbf{F}_{N-1}\\ \mathbf{F}_N\end{Bmatrix}}_{\{\mathbf{F}\}} = \underbrace{\frac{1}{2h}\begin{bmatrix}-2 & 2 & & & & & \\ -1 & 0 & 1 & & & & \\ & -1 & 0 & 1 & & & \\ & & \ddots & \ddots & \ddots & & \\ & & & -1 & 0 & 1 & \\ & & & & -2 & 2 & \end{bmatrix}}_{\mathbf{D}} \underbrace{\begin{Bmatrix}\mathbf{u}_1\\ \mathbf{u}_2\\ \mathbf{u}_3\\ \vdots\\ \mathbf{u}_{N-1}\\ \mathbf{u}_N\end{Bmatrix}}_{\{\mathbf{u}\}} \tag{38}$$

where $\mathbf{u}_i, \mathbf{F}_i$ are the values at node x_i.

Appendix C: Optimality conditions

Set the first term in Eq. 18 to be

$$\Phi(\mathbf{F},\mathbf{u}) = \sum_i \int_{\Omega_i} |f(\mathbf{X}) - g\left(\mathbf{X} + \mathbf{u}_i + (\mathbf{F}_i(\mathbf{X} - \mathbf{X}_{i0}))\right)|^2 d\mathbf{X}. \tag{39}$$

The necessary and sufficient optimality conditions for the ALDIC ADMM formulation are primal feasibility

$$\begin{bmatrix}\mathbf{D}\hat{\mathbf{u}}^* - \mathbf{F}^*\\ \hat{\mathbf{u}}^* - \mathbf{u}^*\end{bmatrix} = \begin{bmatrix}\mathbf{0}\\ \mathbf{0}\end{bmatrix} \tag{40}$$

and dual feasibility,

$$\begin{bmatrix}\frac{\partial\Phi(\mathbf{F}^*,\mathbf{u}^*)}{\partial\mathbf{F}}\\ \frac{\partial\Phi(\mathbf{F}^*,\mathbf{u}^*)}{\partial\mathbf{u}}\end{bmatrix} - \begin{bmatrix}\beta\mathbf{W}^*\\ \mu\mathbf{v}^*\end{bmatrix} = \begin{bmatrix}\mathbf{0}\\ \mathbf{0}\end{bmatrix}. \tag{41}$$

Since $\mathbf{F}^{k+1}, \mathbf{u}^{k+1}$ minimize $\mathcal{L}(\mathbf{F}, \mathbf{u}, \hat{\mathbf{u}}^k, \mathbf{W}^k, \mathbf{v}^k)$ in the ADMM Subproblem 1, we have that

$$\begin{aligned}\begin{bmatrix}\mathbf{0}\\ \mathbf{0}\end{bmatrix} &= \begin{bmatrix}\frac{\partial\Phi(\mathbf{F}^{k+1},\mathbf{u}^{k+1})}{\partial\mathbf{F}}\\ \frac{\partial\Phi(\mathbf{F}^{k+1},\mathbf{u}^{k+1})}{\partial\mathbf{u}}\end{bmatrix} - \begin{bmatrix}\beta\mathbf{W}^k\\ \mu\mathbf{v}^k\end{bmatrix} - \begin{bmatrix}\beta\left(\mathbf{D}\hat{\mathbf{u}}^k - \mathbf{F}^{k+1}\right)\\ \mu\left(\hat{\mathbf{u}}^k - \mathbf{u}^{k+1}\right)\end{bmatrix}\\ &= \begin{bmatrix}\frac{\partial\Phi(\mathbf{F}^{k+1},\mathbf{u}^{k+1})}{\partial\mathbf{F}}\\ \frac{\partial\Phi(\mathbf{F}^{k+1},\mathbf{u}^{k+1})}{\partial\mathbf{u}}\end{bmatrix} - \begin{bmatrix}\beta\mathbf{W}^k\\ \mu\mathbf{v}^k\end{bmatrix} - \begin{bmatrix}\beta\left(\mathbf{D}\hat{\mathbf{u}}^{k+1} - \mathbf{F}^{k+1}\right)\\ \mu\left(\hat{\mathbf{u}}^{k+1} - \mathbf{u}^{k+1}\right)\end{bmatrix} - \begin{bmatrix}\beta\left(\mathbf{D}\hat{\mathbf{u}}^k - \mathbf{D}\hat{\mathbf{u}}^{k+1}\right)\\ \mu\left(\hat{\mathbf{u}}^k - \hat{\mathbf{u}}^{k+1}\right)\end{bmatrix}\\ &= \begin{bmatrix}\frac{\partial\Phi(\mathbf{F}^{k+1},\mathbf{u}^{k+1})}{\partial\mathbf{F}}\\ \frac{\partial\Phi(\mathbf{F}^{k+1},\mathbf{u}^{k+1})}{\partial\mathbf{u}}\end{bmatrix} - \begin{bmatrix}\beta\mathbf{W}^{k+1}\\ \mu\mathbf{v}^{k+1}\end{bmatrix} - \begin{bmatrix}\beta\left(\mathbf{D}\hat{\mathbf{u}}^k - \mathbf{D}\hat{\mathbf{u}}^{k+1}\right)\\ \mu\left(\hat{\mathbf{u}}^k - \hat{\mathbf{u}}^{k+1}\right)\end{bmatrix}.\end{aligned} \tag{42}$$

Or equivalently,

$$\begin{bmatrix}\frac{\partial\Phi(\mathbf{F}^{k+1},\mathbf{u}^{k+1})}{\partial\mathbf{F}}\\ \frac{\partial SSD(\mathbf{F}^{k+1},\mathbf{u}^{k+1})}{\partial\mathbf{u}}\end{bmatrix} - \begin{bmatrix}\beta\mathbf{W}^{k+1}\\ \mu\mathbf{v}^{k+1}\end{bmatrix} = \begin{bmatrix}\beta\left(\mathbf{D}\hat{\mathbf{u}}^k - \mathbf{D}\hat{\mathbf{u}}^{k+1}\right)\\ \mu\left(\hat{\mathbf{u}}^k - \hat{\mathbf{u}}^{k+1}\right)\end{bmatrix}. \tag{43}$$

This means that the quantity

$$\mathbf{s}^{k+1} = \begin{bmatrix}\beta\left(\mathbf{D}\hat{\mathbf{u}}^k - \mathbf{D}\hat{\mathbf{u}}^{k+1}\right)\\ \mu\left(\hat{\mathbf{u}}^k - \hat{\mathbf{u}}^{k+1}\right)\end{bmatrix} \tag{44}$$

can be viewed as a residual for the dual feasibility condition (41). We will refer to $\mathbf{s}^{k+1}$ as the dual residual at ADMM iteration $k+1$, and to

$$\mathbf{r}^{k+1} = \begin{bmatrix}\mathbf{D}\hat{\mathbf{u}}^{k+1} - \mathbf{F}^{k+1}\\ \hat{\mathbf{u}}^{k+1} - \mathbf{u}^{k+1}\end{bmatrix} \tag{45}$$

as the primal residual at ADMM iteration $k+1$. And these two residuals converge to zeros as ADMM proceeds.

References

1. Hild F, Roux S (2006) Digital image correlation: from displacement measurement to identification of elastic properties-a review. Strain 42:69–80
2. Pan B, Qian K, Xie H, Asundi A (2009) Two-dimensional digital image correlation for in-plane displacement and strain measurement: a review. Meas Sci Technol 20:062001
3. Sutton MA, Orteu JJ, Schreier HW (2009) Image correlation for shape, motion and deformation measurements: basic concepts, theory and applications. Springer, Berlin
4. Sutton MA, Wolters WJ, Peters WH, Ranson WF, McNeill SR (1983) Determination of displacements using an improved digital correlation method. Image Vis Comput 1:133–139
5. Chen DJ, Chiang FP, Tan YS, Don HS (1993) Digital speckle-displacement measurement using a complex spectrum method. Appl Opt 32:1839–1849
6. Dhir SK, Sikora JP (1972) An improved method for obtaining the general-displacement field from a holographic interferogram. Exp Mech 12:323–327
7. Kreis T (1996) Holographic interferometry: principles and methods. In: Simulation and experiment in laser metrology: proceedings of the international symposium on laser applications in precision measurements Held in Balatonfured/Hungary, June 3-6, 1996, volume 2. John Wiley & Sons, p 323
8. Rastogi PK (2000) Principles of holographic interferometry and speckle metrology. In: Photomechanics. Springer, pp 103–151
9. Dickinson AS, Taylor AC, Ozturk H, Browne M (2011) Experimental validation of a finite element model of the proximal femur using digital image correlation and a composite bone model. J Biomech Eng 133:014504
10. Franck C, Hong S, Maskarinec SA, Tirrell DA, Ravichandran G (2007) Three-dimensional full-field measurements of large deformations in soft materials using confocal microscopy and digital volume correlation. Exp Mech 47:427–438
11. Franck C, Maskarinec SA, Tirrell DA, Ravichandran G (2011) Three-dimensional traction force microscopy: a new tool for quantifying cell-matrix interactions. PloS one 6:e17833
12. Rehrl C, Kleber S, Antretter T, Pippan R (2011) A methodology to study crystal plasticity inside a compression test sample based on image correlation and ebsd. Mater Charact 62:793–800
13. Daly S (2007) Deformation and fracture of thin sheets of nitinol. Phd thesis California Institute of Technology
14. Bastawros AF, Bart-Smith H, Evans AG (2000) Experimental analysis of deformation mechanisms in a closed-cell aluminum alloy foam. J Mech Phys Solids 48:301–322
15. Jerabek M, Major Z, Lang RW (2010) Strain determination of polymeric materials using digital image correlation. Polym Test 29:407–416
16. Wang Y, Cuitiño AM (2002) Full-field measurements of heterogeneous deformation patterns on polymeric foams using digital image correlation. Int J Solids Struct 39:3777–3796
17. Zdunek J, Brynk T, Mizera J, Pakieła Z, Kurzydłowski KJ (2008) Digital image correlation investigation of portevin–le chatelier effect in an aluminium alloy. Mater Charact 59:1429–1433
18. Tracy J, Waas A, Daly S (2015) Experimental assessment of toughness in ceramic matrix composites using the j-integral with digital image correlation part i: methodology and validation. J Mater Sci 50:4646–4658
19. Kimiecik M, Jones JW, Daly S (2013) Quantitative studies of microstructural phase transformation in nickel-titanium. Mater Lett 95:25–29
20. Chang S, Wang CS, Xiong CY, Fang J (2005) Nanoscale in-plane displacement evaluation by afm scanning and digital image correlation processing. Nanotechnology 16:344
21. Erten E, Reigber A, Hellwich O, Prats P (2009) Glacier velocity monitoring by maximum likelihood texture tracking. IEEE Trans Geosci Remote Sens 47:394–405
22. Rubino V, Lapusta N, Rosakis A (2012) Laboratory earthquake measurements with the high-speed digital image correlation method and applications to super-shear transition. In AGU Fall Meeting Abstracts 1:06
23. Rubino V, Lapusta N, Rosakis AJ, Leprince S, Avouac JP (2014) Static laboratory earthquake measurements with the digital image correlation method. Exp Mech, pp 1–18
24. Besnard G, Leclerc H, Hild F, Roux S, Swiergiel N (2012) Analysis of image series through global digital image correlation. J. Strain Anal Eng Des 47:214–228
25. Blaber J, Adair B, Antoniou A (2015) Ncorr: open-source 2d digital image correlation matlab software. Exp Mech: 1–18
26. Jones EMC, Silberstein MN, White SR, Sottos NR (2014) In situ measurements of strains in composite battery electrodes during electrochemical cycling. Exp Mech 54:971–985
27. Pan B, Wang B, Lubineau G, Moussawi A (2015) Comparison of subset-based local and finite element-based global digital image correlation. Exp Mech 55:887–901
28. Correlated Solutions (2009) Vic-2d Reference Manual
29. Pan B, Asundi A, Xie HM, Gao JX (2009) Digital image correlation using iterative least squares and pointwise least squares for displacement field and strain field measurements. Opt Lasers Eng 47:865–874
30. Avril S, Feissel P, Pierron F, Villon P (2009) Comparison of two approaches for differentiating full-field data in solid mechanics. Meas Sci Technol 21:015703
31. Zhao JQ, Zeng P, Pan B, LP Lei HFDu, He WB, Liu Y, Xu YJ (2012) Improved hermite finite element smoothing method for full-field strain measurement over arbitrary region of interest in digital image correlation. Opt Lasers Eng 50:1662–1671
32. Modersitzki J (2004) Numerical methods for image registration. Oxford University Press, London
33. Ronovskỳ A, Vašatová A (2017) Elastic image registration based on domain decomposition with mesh adaptation. Mathematical Analysis and Numerical Mathematics 15:322–330
34. Bouclier R, Passieux JC (2017) A domain coupling method for finite element digital image correlation with mechanical regularization application to multiscale measurements and parallel computing. Int J Numer Methods Eng 111:123–143
35. Merta M, Vašatová A, Hapla V, Horák D (2014) Parallel implementation of Total-FETI DDM with application to medical image registration. In: Domain Decomposition Methods in Science and Engineering XXI. Springer, pp 917–925
36. Passieux JC, Perie JN, Salaun M (2015) A dual domain decomposition method for finite element digital image correlation. Int J Numer Methods Eng 102:1670–1682
37. Wang TY, Qian KM (2017) Parallel computing in experimental mechanics and optical measurement: a review (ii) Optics and Lasers in Engineering
38. Nocedal J, Wright S (2006) Numerical optimization. Springer, Berlin
39. Conn AR, Gould NIM, Toint PL (1991) A globally convergent augmented Lagrangian algorithm for optimization with general constraints and simple bounds. SIAM J Numer Anal 28:545–572
40. Afonso MV, Bioucas-Dias JM, Figueiredo MAT (2011) An augmented Lagrangian approach to the constrained optimization formulation of imaging inverse problems. IEEE Trans Image Process 20:681–695
41. Simo JC, Laursen TA (1992) An augmented Lagrangian treatment of contact problems involving friction. Comput Struct 42:97–116
42. Michel JC, Moulinec H, Suquet P (2000) A computational method based on augmented Lagrangians and fast Fourier Transforms

for composites with high contrast. CMES-Computer Modeling in Engineering & Sciences 1:79–88
43. Goldstein T, O'Donoghue B, Setzer S, Baraniuk R (2014) Fast alternating direction optimization methods. SIAM J Imag Sci 7:1588–1623
44. Boyd S, Parikh N, Chu E, Peleato B, Eckstein J (2010) Distributed optimization and statistical learning via the alternating direction method of multipliers. Mach Learn 3:1–122
45. Yang JF, Zhang Y (2011) Alternating direction algorithms for l(1)-problems in compressive sensing. SIAM J Sci Comput 33:250–278
46. Afonso MV, Bioucas-Dias JM, Figueiredo MAT (2010) Fast image recovery using variable splitting and constrained optimization. IEEE Trans Image Process 19:2345–2356
47. Glowinski R, Le Tallec P (1989) Augmented Lagrangian and operator-splitting methods in nonlinear mechanics SIAM
48. Pan B, Xie H, Wang Z (2010) Equivalence of digital image correlation criteria for pattern matching. Applied optics 49:5501–5509
49. Simon B, Iain M (2004) Lucas-kanade 20 years on a unifying framework. International journal of computer vision 56:221–255
50. Réthoré J, Hild F, Roux S (2007) Shear-band capturing using a multiscale extended digital image correlation technique. Comput Methods Appl Mech Eng 196:5016–5030
51. Réthoré J, Hild F, Roux S (2008) Extended digital image correlation with crack shape optimization. International Journal for Numerical Methods in Engineerin 73:248–272
52. Reu PL, Toussaint E, Jones E, Bruck HA, Iadicola M, Balcaen R, Turner DZ, Siebert T, Lava P, Simonsen M (2017) Dic challenge developing images and guidelines for evaluating accuracy and resolution of 2d analyses experimental mechanics
53. Bornert M, Doumalin P, Dupré JC, Poilâne C, Robert L, Toussaint E, Wattrisse B (2017) Shortcut in DIC error assessment induced by image interpolation used for subpixel shifting. Opt Lasers Eng 91:124–133
54. Avellar L, Ravichandran G (2016) Deformation and fracture of 3d printed heterogeneous materials Society for Experimental Mechanics Annual Conference
55. Hackbusch W (2003) Multi-grid method and applications. Springer, Berlin
56. Yang J, Bhattacharya K (2018) Combining image compression with digital image correlation. Experimental Mechanics
57. Yang J, Bhattacharya K (2019) Fast adaptive global digital image correlation. In: Advancement of Optical Methods & Digital Image Correlation in Experimental Mechanics, volume 3. Springer, pp 69–73